Imperfect Fabry-Perot resonators

Klaassen, T.

CHAPTER 4

Resonant trapping of scattered light in a degenerate resonator

We demonstrate and discuss the formation of an intriguing interference fringe pattern that is visible in stable resonators at resonator lengths corresponding to a higher-order frequency-degeneracy. The optical trajectories that form these fringes are described for arbitrary degeneracy; the fringes can be used to visualize and quantify imaging aberrations of the cavity relative to a cavity consisting of ideal mirrors.

4.1 Introduction

In textbooks [43, 44], two main types of interference rings are presented: rings of equal inclination, visible in, *e.g.*, a planar Fabry-Perot, and rings of equal thickness, often called Newton rings. It is also known that under certain conditions a third type of interference rings can be observed in the transmission pattern of a multi-transverse-mode Fabry-Perot cavity with spherical mirrors [19,45,46]. For cavity lengths close to frequency-degeneracy rings are observed that are formed by interference in closed optical paths and are resonantly trapped; we dub these "rings of equal (multiple) round-trip path length".

Such interferograms of Fabry-Perot cavities have already been demonstrated in the sixties [19, 45, 46], but only for special cases and generally only for plane-wave illumination. Concentric cavities, which reproduce the optical field on a single round-trip, are discussed by Arnaud [47]. Confocal cavities, which reproduce the field after two round-trips, are discussed by, a.o., Hercher [19] and Bradley and Mitchell [45]. Cavities with other, more general, degeneracies have, however, not been studied to our knowledge.

In this Chapter, we generalize the description of the interferograms for the confocal resonator to resonators, which reproduce the optical field after an *arbitrary* integer number of round-trips (arbitrary degeneracy), including the effect of spherical aberration. We explain the observed interference fringes with a similar approach as Bohr used to explain the discrete levels in atomic systems [48]: we use a ray description to find the optical path (Fermat's principle) and impose the wave criterium that the N-fold round-trip path length should equal a multiple wavelengths.

As an example, we have chosen (arbitrarily) a 6-fold degeneracy cavity. As compared to the earlier work [19, 45, 46], where plane wave, *i.e.*, wide-beam, illumination is used, we use *localized* illumination with a narrow beam. Although we dominantly excite the TEM_{00}-mode, we still observe, surprisingly, weak interference fringes spread over the full mirror aperture. This is due to scattering at the mirrors. This indirect illumination offers a crucial advantage over wide-beam illumination as the resulting fringe pattern is stationary and hardly sensitive to variations in the cavity length. We demonstrate how the fringe pattern can be used to visualize and quantify the imaging aberrations of the cavity. In particular, we demonstrate how the use of higher-order degeneracies allows one to increase the sensitivity for global deformations, like astigmatism, up to accuracies of $\lambda/1000$.

In Section 4.2, we introduce the experiment and describe the formation of the fringe pattern. A generalization of the ray description to arbitrary degeneracy is discussed in Section 4.3. In Section 4.4, we present an application of the interference patterns for very accurate measurement of cavity aberrations. We also give a quantitative description of the relation between the observed interference patterns and mirror deviations from the ideal spherical form. In Section 4.5, we propose a potential application. We summarize our work in Section 4.6.

4.2 Experimental setup and fringe formation

Our optical resonator (see Fig. 4.1) consists of two highly reflective mirrors (nominal specification $R > 99.8\%$ and measured finesse $F \approx 1500$) with a radius of curvature of 50 cm and a

diameter of 5 cm. We probe the resonator with a weakly focussed beam of 1.7 mm diameter at a wavelength of 532 nm, produced by a frequency-doubled single-mode Nd:YAG laser, which dominantly excites the TEM_{00}-mode. We use a piezo element to scan (1 s period) the cavity length over a few wavelengths and average over the cavity resonances. One mirror is placed on a high-resolution mechanical translation stage to set the overall cavity length.
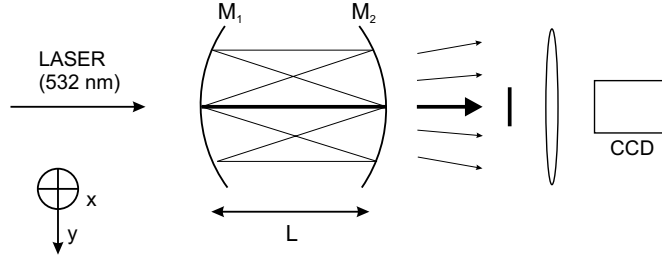

Figure 4.1: *A laserbeam is injected into a symmetric resonator of length L, comprising mirrors M_1 and M_2 of equal radius R. The fringe pattern formed inside the resonator is imaged by a lens onto a CCD-camera. The central ray is obscured to prevent over-exposure of the CCD-camera.*

As frequency-degeneracy plays a crucial role in our experiment, we will first explain this concept on the basis of the Gouy phase. In a wave-optical description, the Gouy phase θ_0 is the round-trip phase delay between the fundamental Hermite Gaussian (HG)-mode as compared to a reference plane wave; higher-order modes (TEM_{mn}) experience a phase delay of $(m+n+1)\theta_0$ [12]. At frequency-degeneracy the Gouy phase is by definition a rational fraction of 2π, $\theta_0 = 2\pi K/N$, with as extreme cases the planar ($K = 0$) and concentric ($K = N$) cavities that operate at the edge of stability. In the ray-optical description, N is the number of longitudinal round-trips that is needed before the ray returns on itself [49], while K represents the number of transverse "oscillations" an orbit makes before closing. For a symmetric cavity, the cavity length L, for which these degenerate points occur, follows from $L = R[1 - \cos(\theta_0/2)]$, where R is the radius of curvature of the mirrors. In this Chapter, we (arbitrarily) chose the degeneracy $K/N = 1/6$, which corresponds to a cavity length $L = 6.7$ cm at $R = 50$ cm. Contrary to the confocal and concentric cavities studied previously [19, 45, 46], our cavity is not at the border of the stability region but well inside [12].

The weak interference fringes, alluded to in Section 4.1, are only observed around frequency-degenerate cavity lengths, where the eigenfrequencies of several eigenmodes overlap. After blocking the on-axis injection beam with a thin obscuration behind the cavity this fringe pattern is imaged by a lens onto a CCD-camera. A typical interference pattern, as observed for a cavity length slightly *longer* than this cavity length, is shown in Fig. 4.2a. The fringes are (almost) circular and the aperture of the mirror is clearly visible. Another pattern, typical for cavities slightly *shorter* than exact degeneracy, is shown in Fig. 4.2b. We attribute the fringes in both these patterns to light that is scattered at the (imperfect) mirror surface out of the injected fundamental mode [50] and resonantly trapped inside the cavity for some specific scattering angles, but not for others.

The advantage of the use of localized over wide-beam illumination is that the fringe pattern is very robust against vibrations; large amounts of scattered light are generated only
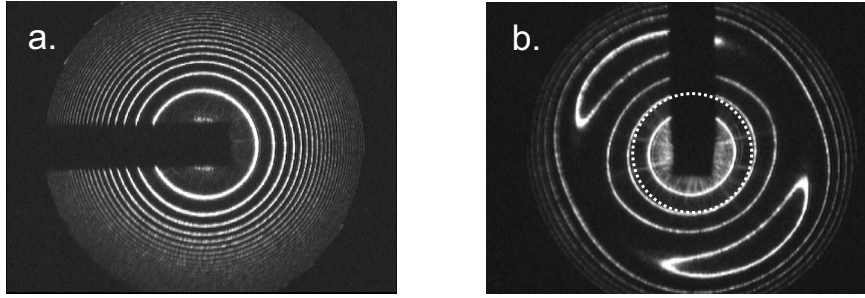
Figure 4.2: *(a) Interference pattern for a cavity tuned slightly longer ($\varepsilon = 50$ μm) than an exact degeneracy of $K/N = 1/6$. The imaged mirror aperture is 5 cm. (b) Interference pattern for a cavity tuned slightly shorter ($\varepsilon = -80$ μm) than an exact degeneracy of $K/N = 1/6$.*

when the cavity length corresponds exactly to a resonance of the fundamental mode. Piezo-scanning of the cavity length leads then to a stroboscopic effect and offers a stationary time-averaged interference pattern. This is contrary to the case of wide-beam illumination which is much more sensitive to vibrations. In that case, there is resonant light present in the cavity for every cavity length: sub-wavelength variations in the cavity length readily wash out the interference pattern, as they lead to shifts of the interference pattern over full fringe distances.

Fig. 4.3 gives a clear demonstration of the buildup of the interference fringes in Fig. 4.2a and b. For clarity, we injected at degeneracy slightly off-axis, which is indicated in Fig. 4.3 by the six bright spots. The piezo, which drives one mirror, is scanned very slowly (100 s period), whereas Fig. 4.2a and b are the result of fast scanning through many resonances. The slow scanning allows us to capture the interference patterns for a specific (almost fixed) cavity length and helps us to visualize the build up of the interference fringes around a single resonance.

Part of the light in the six hit points is scattered into *elliptical* periodic 2D-orbits (see Fig. 4.3) for which only one scatter event is needed. The turning points or vertices of these elliptical orbits form the interference fringes such as shown in Fig. 4.2a and b. The position of the turning points, or equivalently the length of the long axis of the ellipses, is determined by the condition for constructive interference. The total path length of a scatter orbit through the resonator (see Fig. 4.4), of which the hit points on the mirrors are visible as elliptical segments on the mirrors, then has to be a multiple of λ. The ellipses that form the next interference fringe have a total path length which is one λ longer (outside Fig. 4.3). The short axis of the ellipses is determined by the distance between the injection spots out of which the light is scattered.

In the rest of this Chapter, we assume *on-axis* injection, which means that the six injection spots, which were assumed before, now overlap and the scatter ellipses squeeze thus into lines. The fringes are then formed by series of the vertices of *in plane* 1D-orbits. The number of ellipses and the orientation of the ellipses is determined by the precise spatial distribution of the scatter.
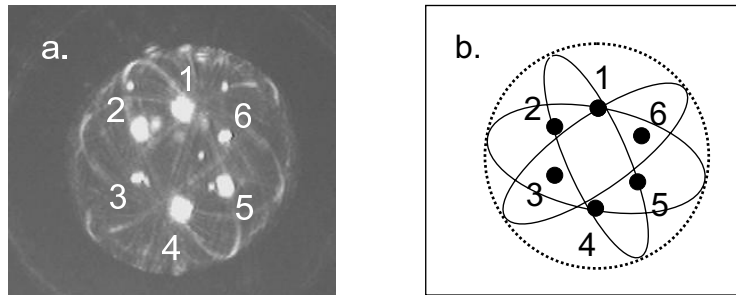
Figure 4.3: *(a) Observation and (b) schematic representation of the buildup of one fringe (m = 1) on the mirror under slow-scan imaging. The 6 bright spots (numbered) are a result of off-axis injection into a N = 6 degenerate cavity. The ellipses are formed by light that is scattered out of the six hit points into periodic orbits. Only the ellipses that interfere constructively after one round-trip (total path length equals λ) are visible. The turning points of the scatter ellipses are observed as the fringe (dotted circle), which has a diameter of 1 cm.*
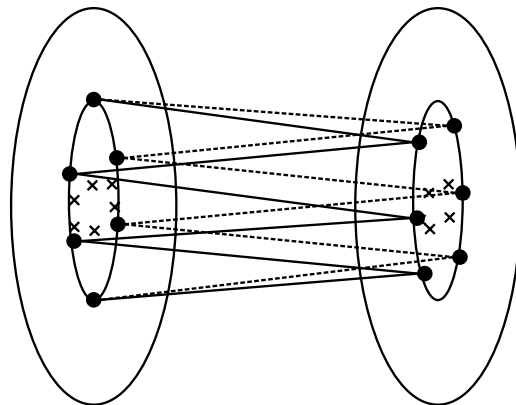

Figure 4.4: *Ray-trace of one periodic orbit through a two-mirror resonator with a degeneracy of N = 6 forming a 2D-ellipse on the mirrors. The hit points of the slightly off-axis injected beam on the mirrors are represented by crosses and the rays in the back are dotted for clarity. The turning points of many of these ellipsis form a fringe in the interference pattern.*

The buildup of the fringes out of elliptical orbits is confirmed by another experiment, where we inserted from *one* side of the resonator a thin obscuration into the cavity. As shown in Fig. 4.5, we observe not *one* but *two* shadows in the fringe pattern, one directly behind the obscuration and the other symmetrically around the optical axis. The obscuration blocks the light scattered out of the injection beam, and obscures a number of ellipses formed out of scattered light. As an ellipse is mirror symmetric around the optical axis, the obscuration of these ellipses appears in the interference fringe patters as *two* shadows.
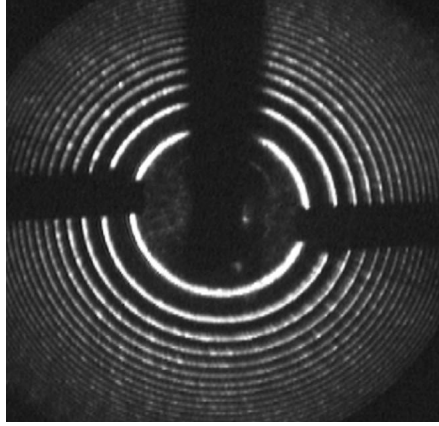

Figure 4.5: *Interference patterns at $\varepsilon = +50\ \mu m$. The vertical shadow is the obscuration outside the resonator blocking the injection beam. The two horizontal shadows are due to a single obscuration inside the resonator.*

4.3   Calculation of "average round-trip path length"

A description of the total round-trip path length in a cavity operating close to an *arbitrary* frequency-degeneracy (including the spherical aberration), other than for the confocal and concentric case, is missing in the literature. In this Section, we will present such expression. We will use a perturbative approach, where we start with the well-known "ABCD-matrix" formalism [12] and add the spherical aberration in a perturbative way by calculating the length of a closed round-trip beyond the second-order expression. We will present a 1D analysis, which properly describes the interference fringes, formed out of the 1D orbits.

For a symmetric two-mirror resonator, we assume that the hit points on the (ideal spherical) mirrors are given by the paraxial form $x_n = \rho \cos(n\theta_0 + \phi_0)$ [49], where $\theta_0 = 2\pi K/N$ is the Gouy phase, ρ is the maximum transverse displacement, and ϕ_0 determines the phase of the first hit point (the ϕ_0 values on the two mirrors differ by $\theta_0/2$). We then calculate the single transit path length $L_{n,n+1}$ between the mirror hit points x_n and x_{n+1} up to fourth order in these transverse displacement. Finally, we average over all x_n values to obtain the average path length

$$\frac{1}{2N}L_{\text{tot}}(\rho) = (L_{\text{res}} + \varepsilon) - B\varepsilon\frac{\rho^2}{R^2} - A\frac{\rho^4}{R^3} \,, \tag{4.1}$$

where $\varepsilon = L - L_{\text{res}}$ is the length detuning away from exact $1/N$-degeneracy and $L_{\text{res}} = R[1 - \cos(\theta_0/2)]$. Note that by Fermat's principle the round-trip path length of the *physical* ray is approximately equal to the length of a nearby closed ray for which the hit points on the mirrors are given by equation mentioned above. The detuning coefficient B and the spherical aberration coefficient A are simple functions of the Gouy phase

$$A = \frac{1 + \cos(\theta_0/2)}{32[1 - \cos(\theta_0/2)]} = \frac{2R - L_{\text{res}}}{32L_{\text{res}}} \quad \text{and} \tag{4.2}$$

$$B = \frac{1}{2}\left[\frac{1}{1 - \cos(\theta_0/2)}\right] = \frac{R}{2L_{\text{res}}} \ . \tag{4.3}$$

Both coefficients are always positive as $L_{\text{res}} < 2R$ for stable resonators and the off-axis path length $L_{\text{tot}}(\rho)$ is thus always smaller than the on-axis path length $L_{\text{tot}}(0)$. The term containing B is the paraxial term (second order in ρ) and the term containing A is the nonparaxial term (fourth order in ρ), which makes L_{tot} a nonparaxial expression.

The above expressions for A and B are only valid for degeneracies with $N \geq 3$, for which the cycle phase ϕ_0 drops out of the averaging $\langle L_{n,n+1} \rangle$. For the confocal case ($N = 2$), the round-trip path length does depend on the cycle phase ϕ_0 [19, 46]. As a result, the "V-type"-orbit has no ρ^4-term whereas the "bowtie"-orbit has an A-coefficient that is twice the value of Eq. 4.2, *i.e.*, $A = 1/16$. For $N = 2$, our general result, Eq. 4.1, thus reduces to the $N = 2$ result of Hercher [19] and Ramsay and Degnan [46], after substitution of the extreme transverse displacements $x_m = \rho \cos(\pi/4) = \rho/\sqrt{2}$.

Fringes appear on the mirrors when the scattered light rays interfere constructively, *i.e.*, when the round-trip path length L_{tot} equals a multiple of a wavelength $n\lambda$ (n is an integer). For $\rho = 0$, we find from Eq. 4.1 the on-axis interference condition: $2N(L_{\text{res}} + \varepsilon) = n_0\lambda$, which gives us for $\rho \neq 0$

$$-2N\left(B\varepsilon\frac{\rho^2}{R^2} + A\frac{\rho^4}{R^3}\right) = (n - n_0)\lambda \ . \tag{4.4}$$

Using $m = n_0 - n$, the fringe radii for various ε can be calculated by rewriting Eq. 4.4

$$\rho_m^2 = R\frac{B}{2A}\left(-\varepsilon \pm \sqrt{\varepsilon^2 + m\lambda 2R\frac{A}{B^2}}\right) \ . \tag{4.5}$$

For $\varepsilon > 0$, ρ_m has only one solution and only for $m > 0$. For $\varepsilon < 0$, Eq. 4.5 has one solution for every $m > 0$ and maximally two solutions for $m < 0$. In the regime where ρ has two solutions, two fringes in the interference pattern fulfill the same interference condition and have the same total path length.

For our specific $N = 6$-configuration, we have calculated the fringe radii for $m \in [-6, 10]$ on the interval $\varepsilon \in [-0.15, 0.17]$ mm using Eq. 4.5, indicated by the solid lines in Fig. 4.6. For $\varepsilon > 0$, it is obvious that every m has only one solution and for $\varepsilon < 0$, m can have two solutions. We also determined the fringe radii as a function of ε experimentally from interference patterns such as shown in Figs. 4.2a and 4.2b, represented by the dots in Fig. 4.6. The excellent agreement of the calculations and measurements confirms our model.
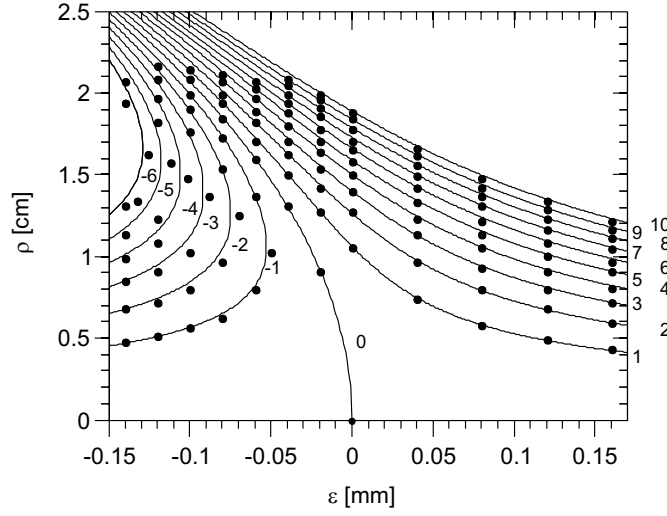
Figure 4.6: *The fringe radius ρ as a function of the distance ε from exact $1/6$-degeneracy. The solid lines are the calculated fringe radii and the dots are the measured fringe radii. There is no adjustable parameter except from a small scaling ($1.14\times$) of the vertical axis to correct for the sharp imaging outside the resonator due to defocussing of the resonator. The numbers in the figure indicate the fringe numbers.*

We noticed that the experimental fringes are imaged sharply in a plane behind the cavity and not on the mirror where the theoretical fringe radii are calculated. The sharp imaging outside the resonator occurs as the rays (of the *physical* path) do not fully coincide, due to intrinsic defocussing of the resonator as described in Eq. 4.1; the fringes are localized where the rays intersect, in our case outside the resonator. That a sharp image of the fringes is not found in the center of the resonator but away from this point has already been mentioned by Bradley *et al.* [45]. We corrected the fringe radii for the diffraction over this distance for a proper comparison (see discussion around Fig. 4.7).

4.4 Aberrations

The transmission interferogram of a cavity composed of two nonspherical mirrors will obviously deviate from that observed or calculated for a cavity with two spherical mirrors. The difference between these interferograms is a sensitive measure for the differences between their mirror height profiles as all mirrors are hit N times, where N can be very large. By comparing the observed interferogram with that expected for ideal spherical mirrors (Eq. 4.1), one can easily deduce the position-dependent change in N-fold round-trip path length $\Delta L_{\text{tot}}[\rho \cos(\theta_0/2), \rho \sin(\theta_0/2)]$ via the criterium that for every extra fringe the total path length changes by λ. The relation between this ΔL_{tot}-profile and the actual height profiles $h_i(\vec{r})$, by which the two mirrors deviate from their ideal spherical reference, is more complicated due to the zigzag nature of the round-trip path. It involves a summation over all

N hit points on each mirror and can be written as

$$\Delta L_{\text{tot}}(\rho \cos \varphi, \rho \sin \varphi) \;=\; 2 \sum_{n=1}^{N} h_1(x_n, y_n) + h_2(x'_n, y'_n)$$

$$\approx \;\; \frac{2N}{\pi} \int_{-\rho}^{\rho} \frac{h(r \cos \varphi, r \sin \varphi)}{\sqrt{\rho^2 - r^2}} dr \,. \qquad (4.6)$$

The integration in Eq. 4.6 remains 1-dimensional as the hit points of the ellipses on each mirror lie on a straight line segment through the origin. This holds for excitation with the fundamental HG-mode only.

The transition from a summation to an integration is valid when the degeneracy N, the cavity finesse F, and the off-axis distance ρ are all sufficiently large to wash out the dependence on the phase $\theta_0/2$ within the transverse oscillations; equivalent to the washing out of the intermediate hit points on the ellipses. This is already the case for the ellipses forming the first fringe ($m = 1$) at exact degeneracy ($\varepsilon = 0$) as shown in Fig. 4.3.

Eq. 4.6 gives the formal link between the combined mirror height profile $h(\vec{r}) = h_1(\vec{r}) + h_2(\vec{r})$ and the deviation $\Delta L_{\text{tot}}(\vec{\rho})$, deduced by comparing the observed interferogram with that expected for ideal spherical mirrors. The inversion of this equation is simple in a Taylor expansion (see below). The integral form already provides for a few basic rules: (i) Only the symmetric part of the function $h(\vec{r})$ survives the (symmetric) integration from $r = -\rho$ to ρ. Any local bump or dip positioned at ρ_0 will show up both at $r = \rho_0$ and at $r = -\rho_0$ as the function $L_{\text{tot}}(\vec{\rho})$ is symmetric in ρ. (ii) The closed round-trip path length $L_{\text{tot}}(\rho)$ is sensitive only to height variations $h(r)$ at $|r| < \rho$. The denominator shows that height variations around $|r| \approx \rho$ have a large weighting factor, as these are the turning points of the transverse oscillation. (iii) The sensitivity of $L_{\text{tot}}(\rho)$ to local height variations $h(r)$, depends on the exact topography of these variations. This sensitivity is better than $\lambda/2$ as each mirror is hit N times during a closed orbit. It is, however, generally smaller than $\lambda/2N$ as the integration corresponds to averaging over the full mirror. The $\lambda/2N$ accuracy is reached only for global mirror deformation that are noticeable all over the mirror surface. The effects of global deformations are best evaluated through a Taylor expansion in position coordinates.

As a check on the validity of Eq. 4.6, we will compare two symmetric cavities, one with spherical mirrors of radii R and the other with mirrors of radii $R + \Delta R$. For this check, we note that the difference ΔL_{tot} in a N-fold round-trip length can be described by both the total path length (Eq. 4.1) and the difference in height profile (Eq. 4.6). The mentioned deformation from mirrors with a radius of curvature of R to $R + \Delta R$ is equivalent to a combined mirror height profile $h[r \cos(\phi), r \sin(\phi)] = -2 \times \frac{\Delta R}{2R^2} r^2$. Substitution of Eq. 4.6 yields a path length change $\frac{1}{2N} \Delta L_{\text{tot}}(\rho) = -\frac{\Delta R}{2R^2} \rho^2$. Alternatively, we can interpret the difference in radii as an extra detuning from the (now different) resonance length $\varepsilon = -\Delta R[1 - \cos(\theta_0/2)] = -\frac{\Delta R}{R} L_{\text{res}}$. Substitution into Eq. 4.1 gives the same path length change as before, which concludes our check.

The center and the outer region of Fig. 4.2b display almost circular fringes. In the intermediate region ($\rho \approx 1.04$ cm) the two patches below and above the injection beam originate from the birth of a "fourth" fringe, counting from the center. The appearance on only the vertical axis clearly demonstrates the presence of mirror astigmatism. The advantage of $\varepsilon < 0$ is that the path length of the N-fold round-trip first increases and then decreases as a function

of the radial distance ρ (see Fig. 4.5), which creates a pattern with a relatively large radial fringe spacing.

To quantify the relation between the interference pattern and the astigmatism of the mirrors, we take a closer look at the labelling of the fringes. The radial dependence of the round-trip path length makes the labelling of the fringes in the vertical direction of Fig. 4.2b, for increasing radial distance: $n = -1, -2, -3, -4, -4, -3, -2, -1, 0, 1, \ldots$. The patches of light labelled with $n = -4$ are thus clamped between the two fringes $n = -3$.

The occurrence of these patches shows that, for a radial distance $\rho = 1.70$ cm off-axis, the difference in the corresponding total round-trip path length is definitely less than two fringes ($\frac{1}{2N}(L_{\text{tot,x}} - L_{\text{tot,y}}) < 2\lambda/12$). This results in a first estimate of the astigmatism of $\Delta R/R < 6.1 \times 10^{-4}$.

We can also determine the astigmatism of the mirrors from the closed inner fringes. The ellipticity of the fringes indicates that the same L_{tot} is found for slightly different off-axis distances ρ. In Fig. 4.2b the ellipticity of fringe $n = -2$ is demonstrated by the tangent inner dotted circle. As the radii of the tangent inner and outer circles differ $(6 \pm 2)\%$ and the radii of the fringes $n = -2$ and $n = -3$ differ by 30% we conclude that the astigmatism at $\rho \approx 0.91$ cm corresponds to a *average* height difference of $[(6 \pm 2)/30]\lambda/2N = (9 \pm 3)$ nm or a relative difference in radii of $\Delta R/R = (2.0 \pm 0.7) \times 10^{-4}$.

The best estimate for the astigmatism is found from a fit of the experimental fringe positions in Fig. 4.7 by $m = a\rho^4 - b\rho^2$ similar to Eq. 4.1, where $a = 2NA/\lambda R^3$ and $b = 2NB\varepsilon/\lambda R^2$. By taking the spherical aberration rotationally symmetric over the mirror we obtain identical fit values $a_x = a_y = 4.80 \times 10^7$. The fitted b is 2.61×10^4 and 2.87×10^4 in the x- and the y-direction, respectively. From these fits we find that $\Delta R/R = (2.30 \pm 0.08) \times 10^{-4}$, so that the radii of curvature differ by $R_x - R_y = (115 \pm 4)$ μm for $R = 50$ cm. This corresponds to a height difference at $\rho = 1.7$ cm of (67 ± 2) nm or an average height difference of $0.75 \times \lambda/12$ fringe spacings.
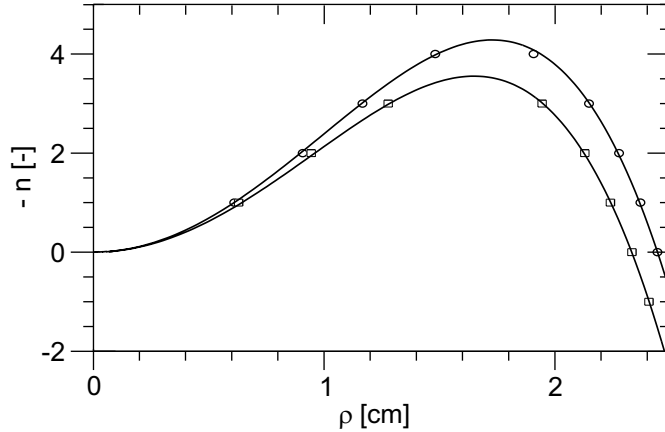

Figure 4.7: *The fringe number as a function of the fringe radius. The upper and lower curve correspond to cuts along the "long" and "short" symmetry axes of Fig. 4.2b.*

It is easy to increase the number of fringes even further by going to a higher-order de-

generacy. A relatively small change in the cavity length (6.70 to 6.28 cm) in fact suffices to go from the $K/N = 1/6$ degeneracy to the $mK/(mN+1) = 5/31$ and thereby increase the number of fringes by roughly an integer factor $m = 5$. The resulting fringe pattern is shown in Fig. 4.8, where the cavity is tuned $\varepsilon \approx -93$ μm away from the degenerate point. The number of fringes in Fig. 4.8 is indeed roughly 5 times as large as in Fig. 4.2 and immediately shows the enhanced sensitivity to average height variations, *i.e.*, $\Delta L/N = \lambda/62$ (an extra fringe appears for every ~ 9 nm average height variation!).
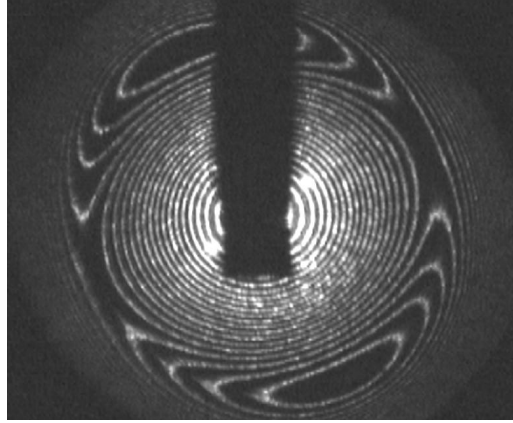

Figure 4.8: *The interference pattern for a degeneracy of $K/N = 5/31$. Due to the higher degeneracy more interference fringes are visible, with spacings corresponding to $\lambda/62$ height variations.*

For proper comparison of the simulated and measured fringe radii, as shown in Fig. 4.6, we have to correct for the diffraction over the distance between the second mirror, where the fringe radii are calculated, and the image-plane of the fringes (6 cm behind the cavity). The comparison of the theoretical and experimental a fitted in Fig. 4.9 can be used for this scaling. As a scales with $1/\rho^4$ (see Eq. 4.1), the magnification of the experimental fringe radii as compared to the theoretical fringe radii ($\rho_{\mathrm{meas}}/\rho_{\mathrm{th}}$) scales with $(a_{\mathrm{th}}/a_{\mathrm{meas}})^{1/4} = (7.97 \times 10^{-4}/4.8 \times 10^{-4})^{1/4} = 1.14\times$. The spatial evolution of the fringe radii due to diffraction inside and outside the resonator (Fig. 4.9) provides us with the same scaling: $1.15\times$.

Finally, we compared the results obtained with our new fringe method with an aberration analysis with a commercially available standard phase-stepped Fizeau interferometer [51–53] (Wyko 400) on which we tested two identical mirrors. The interferograms showed no separated fringes apart from the ones produced by defocus. The phase-stepping technique allowed us to quantify the peak-to-peak height deviation of the individual mirrors, as compared to the spherical reference mirror, to be less than 90 nm within the central aperture of radius $\rho = 1.5$ cm. The astigmatism of each mirror was less than 40 nm peak value in this aperture. Although the values for the astigmatism we found with our fringe method depend on the mutual orientation of the mirrors, the order is comparable with values found with the Fizeau interferometer [51–53].
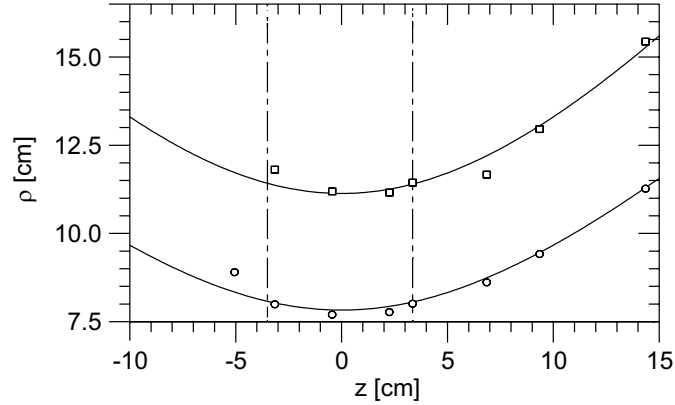
Figure 4.9: *The measured and fitted radii of two fringes for various positions inside and outside the resonator. The dashed-dotted lines represent the mirrors of the resonator.*

4.5 Applications

The described *multi*-beam resonator method may be useful for the accurate inspection of the global aberrations of *single* mode resonators. This may sound surprising, since the cavity length and mirror radii of a single-transverse resonator are such that higher-order transverse modes experience sizeable losses. To study the aberrations in these cavities, we propose to greatly reduce the cavity length, so as to use them in the *multi*-transverse-mode regime. When we then operate the cavity around a higher-order degenerate point with on-axis injection, resonant trapping of scattered light should again produce interferograms like Fig. 4.2. In essence, by greatly shortening the cavity length L and thus increasing the Fresnel number, $N_F = a^2/\lambda L$ [12], where a is the mirror radius and λ the wavelength, we may visualize the resonator aberrations.

An example of a single-mode resonator, where aberrations are a key issue, is the LIGO interferometric gravitational wave detector. The mirrors used in these resonators have to meet very stringent requirements (order $\lambda/2000$ for $R = 7$ km mirrors [7]). Currently, a null wave-front interferometer is used to measure the aberrations of the mirrors. The disadvantage of this method is the required stability for full aperture testing, and the limited aperture capability, where the evolution of LIGO is toward mirrors with even larger radii [54]. Fabrication of such surfaces is a difficult process and our multi-pass method could provide a rapid, full surface scanning of such mirrors, although the limited Finesse of the LIGO interferometer ($F \sim 210$) is still a practical limitation of our method.

4.6 Concluding remarks

We have demonstrated and discussed the formation of fringes in the interference patterns observable around frequency-degenerate cavity lengths. These fringes are the vertices of light that is scattered into closed orbits and resonantly trapped inside the resonator. From this

mechanism we have generalized the total round-trip path length for arbitrary $1/N$ degenerate points. Finally, we have shown how the observed interference pattern can be used for visualization and quantification of cavity aberrations, and possibly applied for testing the mirrors used in gravitational wave detectors.

Appendix (unpublished material)

4.A   Calculation of the total path length

In this Section, the derivation of the total path length in an arbitrary frequency-degenerate cavity ($N > 2$) will be discussed in more detail. We start out calculating the length L of a single pass ray, connecting the hit points on the mirrors P_1 and P_2, as shown in Fig. 4.10. We normalize all (positions and) distances by the identical mirror radii R. The normalized on-
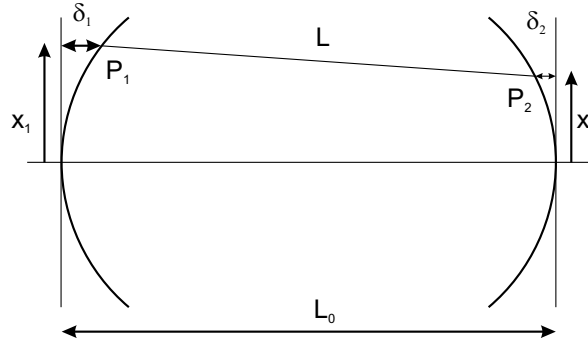

Figure 4.10: *Schematic representation of a ray with a length L connecting the hit points P_1 and P_2 in a frequency-degenerate two-mirror resonator with a cavity length L_0.*

axis cavity length of the frequency-degenerate cavity is $L_0 = L_{\mathrm{res}}/R = 1 - \cos(\theta_0/2)$, where $\theta_0 = 2\pi K/N$ is the round-trip Gouy phase. The (horizontal) distance between the hit points on the mirror and the reference plane is denoted δ.

The length of the ray connecting P_1 and P_2 is given by

$$L = \sqrt{(L_0 - \delta_1 - \delta_2)^2 + (x_2 - x_1)^2} = (L_0 - \delta_1 - \delta_2)\sqrt{1 + \left(\frac{x_2 - x_1}{L_0 - \delta_1 - \delta_2}\right)^2} . \qquad (4.7)$$

In the paraxial limit ($x_1, x_2 \ll L_0$), Eq. 4.7 becomes

$$L \approx (L_0 - \delta_1 - \delta_2) + \frac{(x_2 - x_1)^2}{2(L_0 - \delta_1 - \delta_2)} - \frac{(x_2 - x_1)^4}{8(L_0 - \delta_1 - \delta_2)^3} . \qquad (4.8)$$

Using a Taylor expansion of δ_1 and δ_2 up to the fourth order, *i.e.*,

$$\delta_{1,2} = 1 - \sqrt{1 - x_{1,2}^2} \approx \frac{x_{1,2}^2}{2} + \frac{x_{1,2}^4}{8} , \qquad (4.9)$$

41

we find for Eq. 4.8

$$L \approx L_0 + \frac{(x_2 - x_1)^2}{2L_0} - \frac{x_1^2 + x_2^2}{2} - \frac{x_1^4 + x_2^4}{8} + \frac{(x_2 - x_1)^2 (x_1^2 + x_2^2)}{4L_0^2} - \frac{(x_2 - x_1)^4}{8L_0^3} . \qquad (4.10)$$

We will use this expression to calculate the total path length L_{tot} of a closed orbit in a frequency-degenerate cavity. To do so, we decompose this orbit in $2N$ single passes via $L_{tot} = \sum_{n=0}^{2N-1} L_{n,n+1} = 2N \langle L_{n,n+1} \rangle$. Using Eq. 4.10, the average path length $\langle L_{n,n+1} \rangle$ for a ray connecting two hit points x_n and x_{n+1} can be written as

$$\begin{aligned}
\langle L_{n,n+1} \rangle \quad \approx \quad & L_0 + \frac{\langle (x_{n+1} - x_n)^2 \rangle}{2L_0} - \frac{\langle x_n^2 + x_{n+1}^2 \rangle}{2} - \frac{\langle x_n^4 + x_{n+1}^4 \rangle}{8} \\
& + \frac{\langle (x_{n+1} - x_n)^2 (x_n^2 + x_{n+1}^2) \rangle}{4L_0^2} - \frac{\langle (x_{n+1} - x_n)^4 \rangle}{8L_0^3} .
\end{aligned} \qquad (4.11)$$

For x_n, the unaberrated positions of the hit points are used, found from $x_n = \rho \sin(n\theta_0/2 + \phi_0)$. The eventual extra phase factor ϕ_0 determines the type of orbit, *e.g.*, V-shaped or bow-tie. The relation $x_n = \rho \sin(n\theta_0/2 + \phi_0) = \rho \{ \exp[i(n\theta_0/2 + \phi_0)] - \exp[-i(n\theta_0/2 + \phi_0)] \}/2i$ helps us to simplify Eq. 4.11. Furthermore we use the relation $\langle \exp[i(n\theta_0/2 + \phi_0)] \rangle = 0$, which holds in the case of frequency-degeneracy, where the values $n\theta_0/2$ are equally distributed over the "unit circle" $[0, 2\pi)$. Cycle averages of other powers of x_n and x_{n+1} are calculated by reexpressing products of exponents into sums of exponents with combined arguments followed by a similar cycle average, *e.g.*, $\langle x_n^2 \rangle = \rho^2 \langle \frac{1}{2} + \frac{1}{2} \exp[i(n\theta_0 + 2\phi_0)] \rangle = \rho^2/2$. We note that the phase factor ϕ_0 drops out of all these averages. This means that the total path length for an arbitrary degeneracy ($N > 2$) is independent of the type of orbit. Application of both ideas on the individual terms of Eq. 4.11 results in

$$\begin{aligned}
\langle (x_{n+1} - x_n)^2 \rangle \quad &= \quad \rho^2 [1 - \cos(\theta_0/2)] , & (4.12) \\
\langle x_n^2 + x_{n+1}^2 \rangle \quad &= \quad \rho^2 , & (4.13) \\
\langle x_n^4 + x_{n+1}^4 \rangle \quad &= \quad \tfrac{3}{4} \rho^4 , & (4.14) \\
\langle (x_{n+1} - x_n)^2 (x_n^2 + x_{n+1}^2) \rangle \quad &= \quad \rho^4 \{ \tfrac{1}{2} [\cos(\theta_0/2) - \tfrac{3}{2}]^2 - \tfrac{1}{8} \} , & (4.15) \\
\langle (x_{n+1} - x_n)^4 \rangle \quad &= \quad \tfrac{3}{2} \cos(\theta_0/2)^2 - 3\cos(\theta_0/2) + \tfrac{3}{2} . & (4.16)
\end{aligned}$$

Substitution of Eqs. 4.12–4.16 into Eq. 4.11 finally results in Eq. 4.1, which reads

$$\frac{1}{2N} L_{tot}(\rho) = (L_{res} + \varepsilon) - B\varepsilon \frac{\rho^2}{R^2} - A \frac{\rho^4}{R^3} , \qquad (4.17)$$

where

$$\begin{aligned}
A \quad &= \quad \frac{1 + \cos(\theta_0/2)}{32 [1 - \cos(\theta_0/2)]} = \frac{2R - L_{res}}{32 L_{res}} \quad \text{and} & (4.18) \\
B \quad &= \quad \frac{1}{2} \left[\frac{1}{1 - \cos(\theta_0/2)} \right] = \frac{R}{2 L_{res}} . & (4.19)
\end{aligned}$$

4.B   Evolution of fringes around frequency-degeneracy

For a better understanding of Eq. 4.5, as depicted graphically for $N = 6$ in Fig. 4.6, we discuss here a number of corresponding fringe patterns on the mirror. The intensity profiles for various distances ε away from the exact frequency-degenerate point $N = 7$ are shown in Fig. 4.12. The cavity detuning ε is increased stepwise by 5 μm from $\varepsilon = -55$ to 20 μm. To prevent redundancy, not all pictures out of this series are shown in Fig. 4.12. The astigmatic axis are prominently visible in, a.o., images 1 and 4. The disappearance of the fringes $m = -2, -1$, and 0 can be observed between the images $1 - 2$, $4 - 5$, and in the series of $9 - 12$, respectively. At these points, the transmitted power is redistributed over the mirror. This is shown in Fig. 4.11, where we obscured the on-axis transmitted power and measured the off-axis power as a function of ε. We observe increased transmission exactly at these points, denoted 1, 4, and 9. The radii of the disappearing fringes correspond to $\partial L_{\text{tot}}/\partial \rho = 0$ found from Fermat's principle (see Chapter 6). For those trajectories, the interference of the scattered light is maximally constructive, and the light is "resonantly trapped".
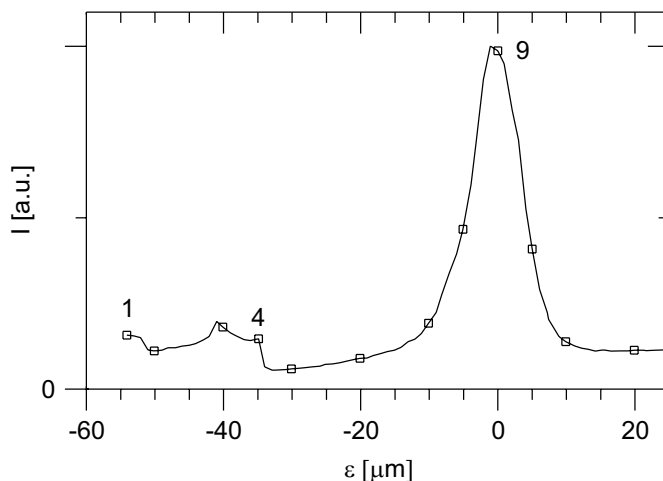

Figure 4.11: *The transmitted power outside the on-axis beam as a function of the cavity detuning. The labelling corresponds to Fig. 4.12. Images 1, 4, and 9 show an increase of the transmitted power (outside the optical axis), corresponding to the "birth" of the fringes $m = -2, -1$ and 0, respectively. The length detuning from image 1 to 4 nicely corresponds to the difference found in the simulations and measurements.*
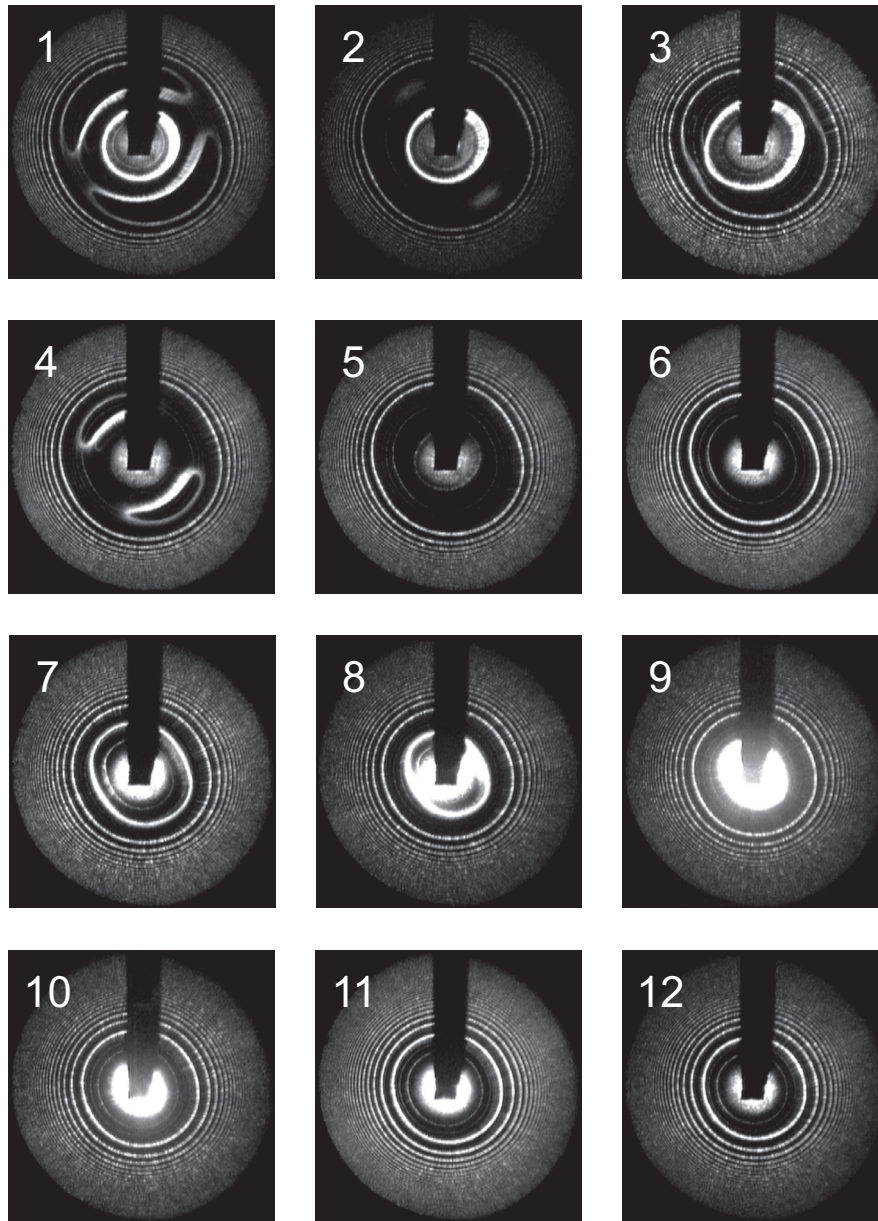
Figure 4.12: *Intensity profiles over the full mirror aperture (diameter 5 cm) around the 7-fold frequency-degeneracy point (N = 7) from $\varepsilon = -55$ (Image 1) to 20 μm (Image 12) in steps of 5 μm (Images at $\varepsilon = -45, -25, -15$ μm and -15 μm are left out). Image 9 represents the fringe pattern at exact frequency-degeneracy ($\varepsilon = 0$) and shows the birth of the m = 0-fringe. To prevent the pictures from overexposure the on-axis beam is blocked.*